Materials Advances

PAPER

Check for updates

Gold nanoparticle-embedded cellulose acetate: structural, optical, mechanical, and cytotoxicity assessment

Mislav Mustapić, [ID] *[a] Maja Molnar, [ID] [b] Nikola Španić, [ID] [c] Mario Komar,[b] Barbara Viljetić,[d] Ljubica Glavaš-Obrovac, [ID] [d] Marija Heffer, [ID] [d] Boštjan Genorio, [ID] [e] Ana Ivković, [ID] [a] Rafael Anelić, [ID] [f] Fabio Faraguna, [ID] [f] Lázár Tóth,[g] Judit Budai, [ID] [g] Zsuzsanna Márton [ID] [g] and Domagoj Belić [ID] *[a]

The development of composites with embedded gold nanoparticles (Au NPs) and biopolymeric matrices, such as cellulose acetate (CA), has gained significant attention due to their unique synergistic properties, including enhanced mechanical, physical, and thermal characteristics. In this study, a composite material consisting of Au NPs embedded in a CA matrix was prepared and thoroughly characterized and its cytotoxicity evaluated for potential medical applications such as drug delivery, biosensing, and imaging. The composite was prepared using a newly developed *in situ* method, ensuring mostly uniform dispersion of Au NPs within the CA matrix. Various characterization techniques, including X-ray diffraction (XRD), scanning electron microscopy (SEM), atomic force microscopy (AFM), energy-dispersive X-ray spectroscopy (EDX), X-ray photoelectron spectroscopy (XPS), UV-Vis spectroscopy, Fourier transform infrared spectroscopy (FTIR), dynamic mechanical analyses (DMA), thermogravimetric analysis (TGA), and cell viability assay were employed to evaluate the structural, mechanical, thermal and biocompatibility properties of the as-prepared composite. The obtained results indicate that even a miniscule content of Au NPs (<0.14 wt%) within the CA matrix can significantly change the properties of such composites. The produced materials are compact, flexible, strong, and exhibit low cytotoxicity, making them suitable for a wide range of potential applications.

Introduction

In recent decades nanotechnology has been one of the most rapidly advancing fields of science and industry due to its broad range of applications across a wide array of disciplines. Its influence spans various sectors, including electronics, mechanics, optics, biomedicine, catalysis, magnetics, energy production, and food technology. Nanotechnology's ability to improve and revolutionize these fields is largely attributed to its manipulation of materials at the nanoscale. One of the most promising areas for nanotechnology is biomedicine, where it is highly interdisciplinary and requires collaboration across medicine, materials science, biotechnology, chemistry, and physics.

Nanoparticles are ideal for a range of biomedical applications, such as targeted drug delivery systems, where their small size and large surface area allow them to interact with biological systems at the molecular level.[1–4]

Au NPs are of particular interest in medicine because of their exceptional biocompatibility, stability, and ability to be functionalized for specific biological applications. Historically, gold has been used in medicine for thousands of years, for treating conditions such as rheumatic diseases and skin inflammations.[5–8] Today, Au NPs are widely utilized in biosensing, diagnostics, and therapeutic applications and as catalysts for various reactions.[9–14] Furthermore, their optical properties, particularly surface plasmon resonance, allow them to be used in highly sensitive diagnostic tools for detecting biomolecules at low concentrations.[15–20]

A new group of materials formed of nanoparticles and biopolymers combine the unique properties of nanoparticles with the advantageous characteristics of biopolymers making them promising for applications in biomedicine, materials science, and engineering. The goal of producing such nanocomposites is to create materials that can replace synthetic

[a] Josip Juraj Strossmayer University of Osijek, Department of Physics, Croatia. E-mail: mmustapic@fizika.unios.hr, dbelic@fizika.unios.hr
[b] Josip Juraj Strossmayer University of Osijek, Faculty of Food Technology, Croatia
[c] University of Zagreb, Faculty of Forestry and Wood Technology, Croatia
[d] Josip Juraj Strossmayer University of Osijek, Faculty of Medicine, Croatia
[e] University of Ljubljana, Faculty of Chemistry and Chemical Technology, Slovenia
[f] University of Zagreb, Faculty of Chemical Engineering and Technology, Croatia
[g] ELI-ALPS, ELI-HU Nonprofit Ltd. Szeged H-6728, Hungary

polymers, especially in the context of biocompatibility and environmental sustainability. Nanocomposite materials also offer synergistic effects, where the combined properties of the different components enhance the material's overall performance, improving structural properties and interfacial characteristics.[21,22]

Cellulose, the most abundant biopolymer on Earth, plays a key role in nanocomposite materials due to its versatility, environmental friendliness, sustainability and biocompatibility.[23–26] Its widespread availability, along with its ability to be functionalized and modified, makes cellulose an ideal matrix material for incorporating nanoparticles. However, to be used as a matrix, in most cases cellulose must be chemically altered to produce more suitable materials, such as CA. As a product of targeted esterification of cellulose, CA is a very versatile material with favourable mechanical, chemical and thermal properties.[27] Its increased hardness, good impact resistance, great optical transparency, and good resistance to hydrocarbons[28] make it a suitable substitution for common fossil-based polymers used to make everyday items (*e.g.* synthetic fibres for clothing, eyeglass frames and toothbrush handles). Additionally, CA is readily soluble in various organic and inorganic solvents and can be blended with other (bio)-polymers, thus making it ideal for various biomedical, pharmaceutical and industrial applications.[29] The interaction between nanoparticles and the cellulose matrix (*e.g.* CA) can be tailored through modifications in nanoparticle size, shape, and surface chemistry, providing additional functional capabilities.[30–37]

One application of nanocomposite materials in the biomedical field is in transdermal drug delivery systems. Transdermal patches offer an alternative method for delivering drugs through the skin, bypassing the digestive system and avoiding the first-pass metabolism in the liver.[2,3,38] This method also avoids the risks associated with intravenous drug delivery, such as infection and pain. The advantages of transdermal drug delivery include the ability to provide controlled and continuous drug release over a prolonged period, as well as the ease of applying and removing the patch from the skin. Transdermal systems are already in use for various medical conditions, including hormone therapy, chronic pain management, smoking cessation, and motion sickness.[39,40]

Recent research shows that cellulose composites modified with Au NPs are promising materials, especially for biomedical applications that require direct and prolonged tissue contact.[41] Such materials benefit from the unique optical and functional properties of Au NPs, including photothermal responsiveness, which is useful for controlled therapeutic delivery and diagnostic applications.[15] In addition, Au NPs incorporated into polymeric matrices enhance mechanical strength and anti-microbial properties, further improving their suitability for medical applications.[42,43] CA, which was chosen as the polymer matrix in this study, provides an optimal basis for long-term biomedical interfaces and ensures durability and structural integrity during prolonged tissue contact.

In this research study we developed and extensively characterized a material for potential transdermal patches made from Au NPs and CA. The Au NPs were incorporated into the CA matrix with various concentrations to tailor the composite's properties, such as its mechanical strength, flexibility, photo-sensitivity, biocompatibility and low toxicity. Furthermore, this new composite showed potential for additional enhancements, such as light, electrical, or ultrasound stimulation, which could be used to improve drug delivery efficacy and control.

CA, on the other hand, was chosen as the matrix material due to its ease of processing, biocompatibility, and ability to form thin flexible films suitable for transdermal patches. By combining these two materials, the new composite not only offers potential for enhanced drug delivery but also for other biomedical applications, such as biosensing, transdermal and photothermal therapy.

Materials and methods

Materials

CA was prepared using Black Alder (*Alnus glutinosa* [L.] Gaertn.) wood as a basic raw material. Black Alder was chosen as it has adequate chemical composition with rather high cellulose content[44] and was sampled in accordance to the TAPPI T257 cm-12 standard.[45] After sampling, the wood was air dried and milled using a Retsch SM 300 cutting mill equipped with a 1 mm bore opening sieve. The prepared wood flour was then sieved using the Retsch AS 200 basic vibratory sieve shaker, and wood flour with particles sized between 0.5 and 1 mm were selected for cellulose isolation and acetylation. Ethanol, nitric acid, toluene, acetic acid and acetic anhydride were purchased from Gram-mol, Croatia.

Sodium citrate dihydrate was purchased from Kemika, Croatia. Perchloric acid was purchased from Merck, Germany. Dichloromethane was purchased from Carlo Erba, Italy. Gold(III) chloride solution was purchased from Sigma Aldrich, USA. All chemicals were of analytical reagent grade. Deionised water used in all parts of the experiment was ASTM type II and prepared using a TKA MicroMed system.

Cellulose isolation

Kürchner–Hoffer cellulose[45,46] was isolated from pre-extracted wood, using an ethanol/nitric acid mixture (4 : 1 v/v%). Wood flour extraction was carried out according to TAPPI T204 cm-97[46] in Soxhlet apparatus using a toluene/ethanol mixture (2 : 1 v/v%). The obtained cellulose was filtered, washed with hot deionised water and dried overnight at 70 °C in order to remove excess water.

Cellulose acetylation

Cellulose acetylation was carried out as described in our earlier paper.[47] Briefly, 100 g of cellulose in a 3000 mL laboratory glass beaker was treated for 1 minute with the reaction mixture consisting of 500 mL acetic acid, 1000 mL of toluene and 5 mL perchloric acid. After 1 minute, 500 mL of acetic anhydride was added to the reaction mixture. Acetylation was carried out at room temperature, and the total acetylation time was 45 minutes (1 + 44 minutes), after which 1000 mL of

deionised water was added in order to precipitate the CA. During acetylation, the reaction mixture was vigorously stirred by means of a IKA Turrax T18 homogeniser paired with an electromagnetic stirrer IKA C-MAG HS7. The obtained CA was then vacuum filtered and alternately washed with ethanol and deionised water (1000 mL portions). The washing was conducted until the final product was scentless. CA was then dried for 8 h at 40 °C in order to remove excess water, re-pulverised and sieved over a 0.2 mm sieve. In this way, one can acquire CA in the form of a white powder. Such CA had 41.17% acetyl and a degree of substitution (DS) of 2.54 as determined according to ASTM D817-96.[48]

Neat CA film

Neat CA film was prepared by the solvent cast method using dichloromethane as the appropriate solvent. The CA powder was dissolved in a glass laboratory beaker, to which a known amount of solvent was added (5 w/v%). The prepared mixture (50 mL) was then poured into a glass Petri dish (φ = 11 cm) that was put on a levelled surface in order to obtain films of uniform thickness. The cast neat CA mixture was left undisturbed in a covered Petri dish for three days at room temperature, during which the solvent slowly evaporated, leaving a compact thin film at the bottom of the dish that can be collected by tweezers.

Composite materials preparation

The synthesis of Au NP – CA composite materials was based on a modified Turkevich method[49] in which the reduction of gold(III) chloride solution with sodium citrate took place in a suspension of CA in water. By changing the molar fraction of the gold(III) chloride and sodium citrate with respect to the volume of suspension of CA in water, one can obtain composite samples with varying content of Au NPs, as described more in detail below.

Sample 1 (S1)

A mixture of deionised water (100 mL) and CA (0.5 g) was stirred in a 500 mL round-bottom flask using a magnetic stirrer for 5 minutes at room temperature. Sodium citrate dihydrate (19.42 mg; 0.066 mmol) was dissolved in 30 mL of deionised water and the resulting solution was added to the suspension of CA. Subsequently, 10 μL of gold(III) chloride solution was diluted with 1990 μL of deionised water and rapidly injected into the mixture under continuous stirring. After 30 minutes the colour changed to dark red, indicating nanoparticle formation. The resulting precipitate was collected by filtration and dried at 50 °C for 4 hours. The dried material was then dissolved in 20 mL of dichloromethane and poured into a Petri dish (φ = 5 cm). The poured mixture was kept at room temperature in the closed Petri dish until dichloromethane fully evaporated, forming a compact thin film at the bottom of the dish.

Sample 2 (S2)

A mixture of deionised water (100 mL) and CA (0.5 g) was stirred in a 500 mL round-bottom flask using a magnetic stirrer for 5 minutes at room temperature. Sodium citrate dihydrate (38.85 mg; 0.132 mmol) was dissolved in 60 mL of deionised water and the resulting solution was added to the suspension of CA. Subsequently, 20 μL of gold(III) chloride solution was diluted with 1980 μL of deionised water and rapidly injected into the mixture under continuous stirring. After 30 minutes the colour changed to dark red, indicating nanoparticle formation. The resulting precipitate was collected by filtration and dried at 50 °C for 4 hours. The dried material was then dissolved in 20 mL of dichloromethane and poured into a Petri dish (φ = 5 cm). The poured mixture was kept at room temperature in the closed Petri dish until dichloromethane fully evaporated, forming a compact thin film at the bottom of the dish.

Sample 3 (S3)

A mixture of deionised water (100 mL) and CA (0.5 g) was stirred in a 500 mL round-bottom flask using a magnetic stirrer for 5 minutes at room temperature. Sodium citrate dihydrate (116.20 mg; 0.395 mmol) was dissolved in 180 mL of deionised water and the resulting solution was added to the suspension of CA. Subsequently, 60 μL of gold(III) chloride solution was diluted with 1940 μL of deionised water and rapidly injected into the mixture under continuous stirring. After 30 minutes the colour changed to dark red, indicating nanoparticle formation. The resulting precipitate was collected by filtration and dried at 50 °C for 4 hours. The dried material was then dissolved in 20 mL of dichloromethane and poured into a Petri dish (φ = 5 cm). The poured mixture was kept at room temperature in the closed Petri dish until dichloromethane fully evaporated, forming a compact thin film at the bottom of the dish.

X-ray diffraction

X-ray diffraction analysis (XRD) was performed using a Bruker D8 Advance device with a Cu Kα radiation under acceleration voltage of 40 kV and current of 25 mA. The scans were taken in Bragg-Brentano configuration comprising a point collimator, between 5 and 80 °2θ, with steps of 0.01 °2θ, and acquisition speed of 5 s per step.

Scanning electron microscopy

The morphology of the samples was studied with a JEOL JSM-6400 scanning electron microscope. In addition, high-resolution imaging of samples (using both secondary and backscattered electrons) was performed using a Thermo Fisher Scios 2 Dual Beam instrument. EDX measurements were performed using a Raith eLINE Plus SEM equipped with a Bruker EDX system. The SEM images were processed using Fiji software.

Atomic force microscopy

Atomic force microscopy (AFM) was performed using a Nano-surf CoreAFM device at room temperature in contact mode (static mode), employing a silicon probe (Tap300Al-G) with a tip radius of 10 nm and a vibration frequency of 300 kHz. Scans were conducted on an area of 10 × 10 μm with an acquisition

time of 0.78 s. The images were processed using Nanosurf software.

X-ray photoelectron spectroscopy

XPS measurements were conducted using a Versa Probe 3 AD (PHI, Chanhassen, USA) equipped with a monochromatic Al Kα X-ray source. The source operated at an accelerating voltage of 15 kV, and 46 W. Powder samples were mounted on double-sided Scotch tape and positioned at the center of the XPS holder. Spectra were acquired for each sample over a 200 × 200 μm analysis area, with the charge neutralizer activated during data collection. Survey spectra were measured using a pass energy of 224 eV and a step size of 0.2 eV. High-resolution (HR) spectra were recorded with a pass energy of 27 eV and a step size of 0.05 eV. To ensure high-quality spectral data with a good signal-to-noise ratio, at least 10 sweeps were performed for each measurement. The energy scale of the XPS spectra and any possible charging effects were corrected by referencing the C=C peak in the C 1s spectrum with a binding energy (BE) of 284.8 eV. Spectral quantification was carried out using MultiPak 9.9.1 software with Shirley background correction. Deconvolution (Fitting) was performed using CasaXPS 2.3.26 software, with a Shirley type background and 70–30% Gaussian–Lorentzian peak shapes.

UV-vis spectroscopy and opacity measurements

Optical properties were investigated using an Ocean Optics USB2000 fibre optics spectrometer with a tungsten–halogen lamp as the light source. Additionally, to supplement these measurements specifically in the ultraviolet (UV) range where the tungsten–halogen lamp has low intensity, a 8 W Philips TL F8T5/BLB UV lamp was used. In addition, opacity of the produced films was calculated based on the absorbance values measured at 550 nm on a Shimadzu UV-mini 1240 spectrophotometer. Film thickness was measured using an INSIZE digital micrometre (model 3100-25; 0.001 mm precision). Mean values of five thickness measurements per sample were used for opacity calculation.

Infrared spectroscopy

Attenuated total reflectance with Fourier transform infrared (ATR-FTIR) spectroscopy analysis of the material was performed on a PerkinElmer FT-IR spectrum one spectrometer in the wavelength range from 650 to 4000 cm^{-1} at a resolution of 4 cm^{-1}.

Thermal and mechanical measurements

Thermogravimetric measurements were performed using a Mettler Toledo TGA/DSC 3+. The analysis was carried out in two steps with different gases: the first step involved heating from 30 to 600 °C in a nitrogen atmosphere, while the second step was heating in an air atmosphere from 600 to 900 °C. The gas flow was set to 30 mL min^{-1} and the heating rate was 10 °C min^{-1}.

Differential scanning calorimetry (DSC) was carried out on a PerkinElmer DSC 6000 by heating and cooling the samples (6–8 mg) from 30 °C to 330 °C, using a scanning rate of 20 °C min^{-1}, under a nitrogen flow of 50 mL min^{-1}. The melting (T_m) and crystallization (T_c) temperatures were taken as the peak temperatures of the melting endotherm and the crystallization exotherm. The value of 58.8 J g^{-1} as the heat of fusion of a perfect crystal of CA was used to determine the degree of crystallinity.[50]

The axial tensile tests were performed using a TA Instruments HR 30 hybrid rheometer with a rectangular axial test fixture. The test was carried out at room temperature (25 °C) with a constant linear strain rate of 5.0 μm s^{-1} until the sample broke. Dynamic mechanical analysis (DMA) was performed using a TA Instruments HR 30 hybrid rheometer with the rectangular axial test fixture. Temperature control was maintained using the supplied TA Instruments environmental test chamber. The measurement parameters were as follows: the initial axial tensile force was set to 1.0 N; the measurement was conducted from 25 to 300 °C with a heating rate of 3 °C min^{-1}. The oscillation frequency was set to 1.0 Hz, while the amplitude was 2.0 μm. The temperature range was chosen to cover the glass transition region around 200 °C and extended up to the onset of degradation. Beyond this temperature, no usable data could be obtained. The tensile force and amplitude were selected based on preliminary tests. A frequency of 1 Hz is commonly specified in material testing standards, making it a valuable baseline for comparing results between different laboratories and materials.

Porosity test

The porosity test was performed according to Wang et al.[51] by immersion of thin strips (prepared as previously described) into deionised water (20 °C) for 1 hour, followed by drying in a vacuum oven at reduced pressure for 4 hours.

Assessment of acetylated cellulose cytocompatibility using MTT assay

Cell viability was assessed using the MTT assay (3-(4,5-di-methylthiazol-2-yl)-2,5-diphenyl tetrazolium bromide), which detects mitochondrial dehydrogenase activity in viable cells.[52] The assay was performed using the human fetal lung fibroblast cell line (MRC-5), at a density of 2×10^4 cells per well in 96-well flat-bottom plates (Greiner, Frickenhausen, Austria). Cells growing in a monolayer were cultured in Dulbecco's Modified Eagle's Medium (DMEM; Gibco, Thermo Fisher Scientific Inc., Waltham, MA, USA) supplemented with 2 mM glutamine, 10% heat-inactivated fetal bovine serum (FBS, Gibco, Thermo Fisher Scientific Inc., Waltham, MA, USA), and antibiotics (100 U mL^{-1} penicillin and 0.1 mg mL^{-1} streptomycin). The cells were grown in a CO$_2$ incubator (IGO 150 CELLlife™, JOUAN, Thermo Fisher Scientific, Waltham, MA, USA) in a humidified atmosphere containing 5% CO$_2$ at 37 °C.

Prior to in vitro assay, neat CA and composite samples were punched into discs with a diameter of 3 mm and sterilized under UV light. For the MTT assay, plates were placed in wells with cells and incubated for 48 hours. Following the incubation period, the culture medium was removed, and 40 μL of MTT solution (5 mg mL^{-1}) was added to each well. Samples were

incubated for an additional 4 hours at 37 °C to allow the formation of formazan crystals.

After incubation, 160 μL of dimethyl sulfoxide (DMSO) was added to each well to dissolve the formazan crystals. Next, the solutions were transferred into a new 96-well plate, and absorbance was measured at 595 nm using an iMark microplate reader (Bio-Rad, Hercules, CA, USA). Results are presented as a percentage of viable cells incubated with composites compared to control cells incubated with non-modified CA (set to 100%).

Results and discussion

X-ray diffraction analysis

The neat CA and composite samples S1, S2, and S3 (prepared by progressively increasing the content of Au NPs) were firstly investigated by XRD (Fig. 1). The acquired XRD patterns revealed that composite samples had higher crystallinity than neat CA. All samples showed a common crystalline phase that could be assigned to triacetylcellulose (ICDD PDF #03-0021). In addition, crystalline gold (ICDD PDF#04-0784) could be

Fig. 1 XRD patterns of all samples.

Fig. 2 SEM images (top view) of the neat CA and composite samples S1, S2, and S3.

identified, most notably in sample S3. On the other hand, XRD patterns of samples S1 and S2 indicated a very low concentration of crystalline Au, all in line with the expectations based on the syntheses conditions. In general, the presence of both phases is in accordance with the used precursors and conducted chemical syntheses. Considering the statistical nature of the XRD method and the relatively large interaction volume, it is also possible that a few large crystals formed during the evaporation of the precursor solution in samples CA and S2, perhaps due to slight variations in syntheses conditions. It is well known that cellulose-based materials can crystallize in multiple forms. Namely, the two mentioned samples show an additional peak (highlighted in Fig. 1, at $°2\theta = 32.3$) indicating the presence of another crystalline phase. This peak could be attributed to the increase in the interfibrillar distance induced by the presence of acetyl groups within cellulose chains,[52] or it can be associated with parts of amorphous structures of residual lignin and hemicelluloses, still present in Kürchner–Hoffer cellulose after its isolation.[53–56] The absence of this peak in patterns of samples S1 and S3 is an indication of a complete lignin and hemicelluloses removal due to prolonged chemical treatment. In addition, because the Turkevich method itself is highly sensitive to variations in parameters, other minor (crystalline) by-products could have been made in the modified synthesis.[57,58]

Surface morphology and composition

The morphological characterization of samples was performed using scanning electron microscopy (SEM), which revealed Au NPs embedded into the CA matrix (Fig. 2). The topography analysis suggested that the surface becomes increasingly rougher with increasing concentration of Au NPs. This indicates that the incorporation of Au nanoparticles significantly changes the surface properties of the composite material, meaning that certain functional properties of CA materials could be tailored by the addition of Au NPs. For example, the roughened surface can provide a larger active surface area, which is particularly beneficial in applications such as biosensors, where surface interactions with biological molecules are critical, or drug delivery systems, where improved adhesion and release properties are desired. Also, rough surfaces can serve as active sites for heterogeneous catalysis or other interaction-driven applications due to larger surface area. The interplay between uniform dispersion, local agglomeration and altered surface topography illustrates the complex yet tuneable nature of these composites, making them promising candidates for advanced technological and biomedical applications.

This low-resolution observation is further supported by the high-resolution SEM imaging using backscattered electrons, which provided a strong contrast between the Au NPs and the CA matrix, allowing for clear visualization of individual NPs (Fig. 3). The obtained images suggest that Au NPs are indeed relatively sparsely distributed within the CA matrix. What is more, based on the images, one can estimate the size of the Au NPs to be in the range of 10 to 20 nm (Fig. 3 c), in good agreement with the expectation based on the synthesis
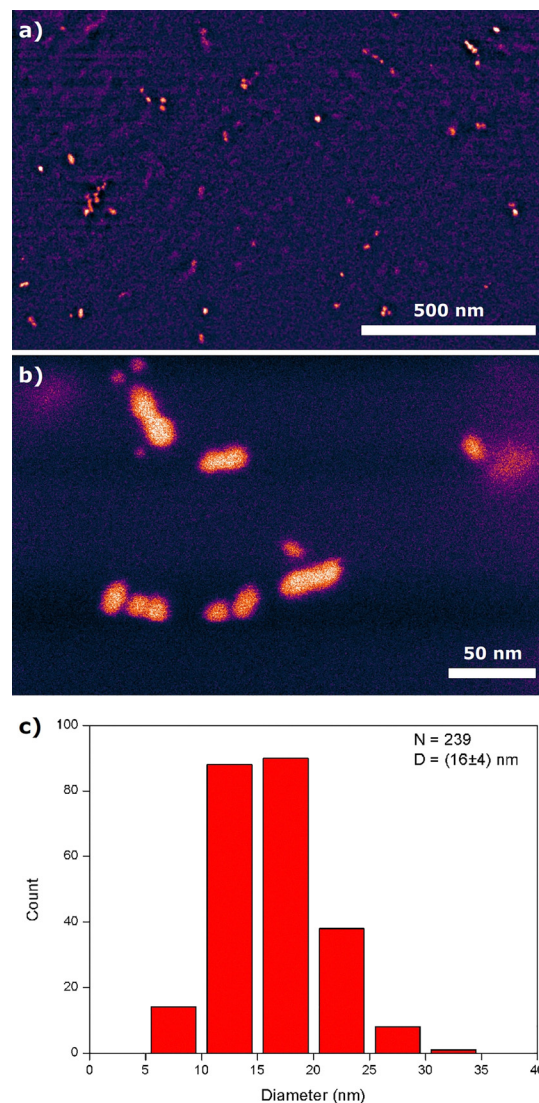

Fig. 3 High-resolution SEM images (backscattered signal, false colour) of sample S3: (a) magnification 100 000×; (b) magnification 500 000×. (c) Size distribution of Au NPs in sample S3, based on high-resolution SEM images comprising 239 Au NPs in total.

parameters. According to clear observation of 239 Au NPs from 8 HRSEM images, statistical analysis revealed the Au NP size of (16 ± 4) nm in diameter (assuming perfectly spherical particles). It should be noted though that the SEM signal suffers from certain delocalization, so that the true NP size could be a bit smaller.

To further assess the surface properties of samples, AFM was utilized. AFM scans (Z scans) more clearly illustrated the evolution of the roughness of surfaces from the CA to the composite samples, as shown in Fig. 4. To facilitate the comparison among the samples, both 2 D and 3D representative surface views are presented. Scanned areas clearly showed an increasing trend for surface root mean square (RMS) roughness (Table 1) with the rising Au NP content. The increase of surface RMS roughness is gradual, which is very likely the
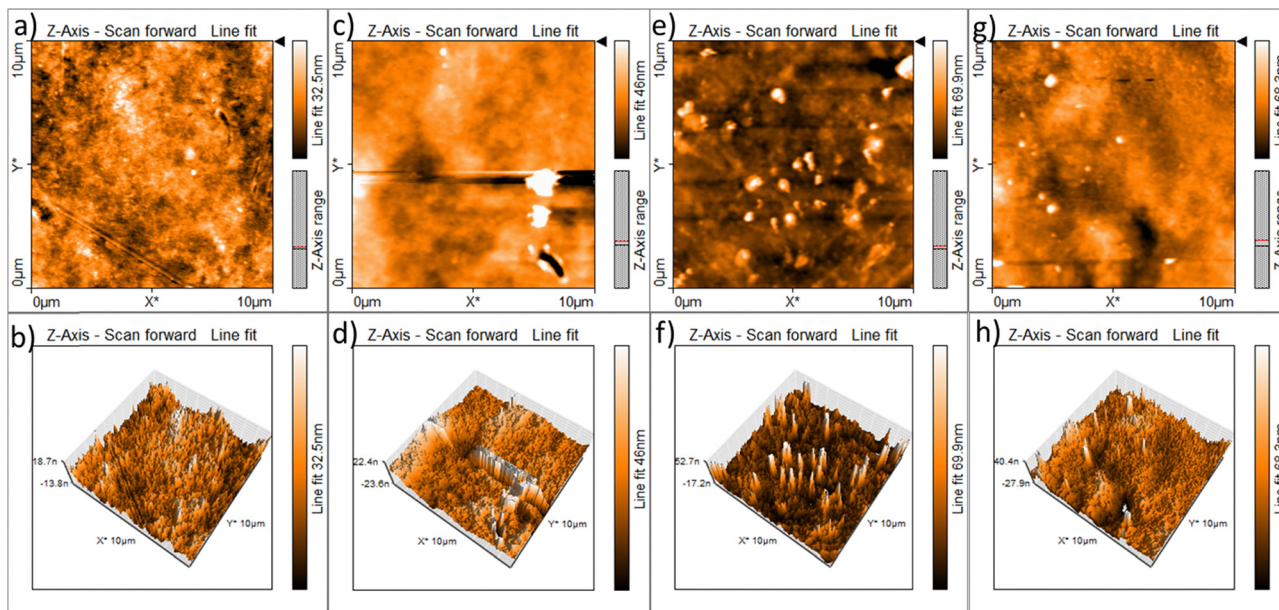
Fig. 4 AFM images the neat CA and composites S1, S2, and S3: Z-scan 2D (a) and 3D (b) of sample CA; Z-scan 2D (c) and 3D (d) of sample S1; Z-scan 2D (e) and 3D (f) of sample S3; Z-scan 2D (g) and 3D (h) of sample S3.

Table 1 Surface RMS roughness values for all samples

Sample	RMS/nm
CA	5.03
S1	12.90
S2	18.37
S3	25.04

consequence of growth-related transformations in the samples related to the addition of Au NPs.

The surface composition was further analysed by EDX (Fig. 5) and XPS (Fig. 6), which confirmed that the predominant chemical components of the surface were carbon and oxygen, at (59 ± 6) wt% and (47 ± 5) wt%, respectively, in all the samples, originating from the CA matrix. The gold content remained below the EDX detection limit (<0.1 wt%) for samples S1 and S2; only sample S3 gave a small but detectable gold signal of (0.13 ± 0.04) wt%. Similarly, XPS measurements indicated the presence of gold only in sample S3 – the one with the highest nominal gold concentration, but again just in traces. As a side note, some silicon was detected by XPS as a contaminant, possibly introduced during sample preparation or handling. Combined, the EDX and XPS results indicate that the fraction of gold in the composite samples is miniscule.

The absence of surface gold at lower concentrations supports the assumption of a well-dispersed system where the

Fig. 5 EDX elemental mapping of sample S3: (a) carbon; (b) oxygen; (c) gold; (d) combined signal (overlaid on the secondary electron image).
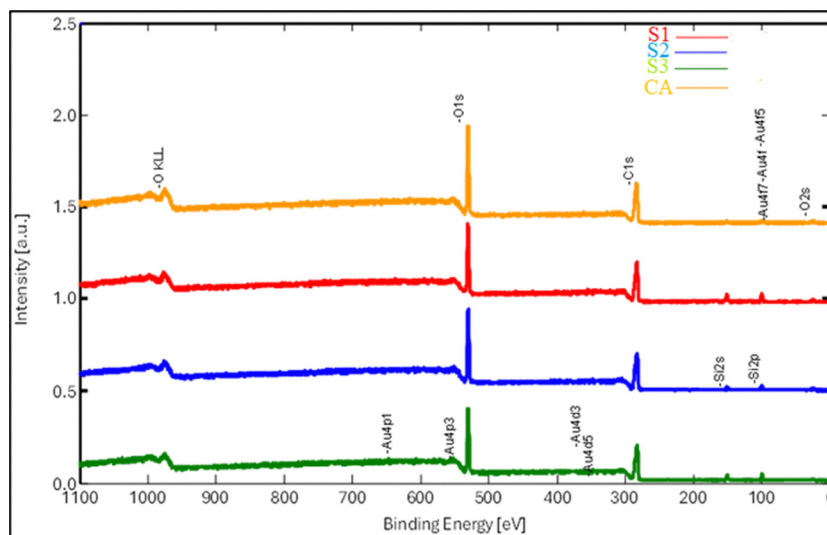
Fig. 6 XPS survey spectra of the neat CA and composites S1, S2, and S3.

nanoparticles are effectively encapsulated in the polymer matrix. In general, such an encapsulated arrangement of metal nanoparticles is critical for applications that require oxidation protection for the metal, while simultaneously utilizing the functional properties of the embedded nanoparticles. This design ensures the longevity and stability of the metal components, especially in environments prone to oxidation, while maintaining the structural integrity and functional versatility of the composite material.

UV-vis spectroscopy, FTIR spectroscopy and porosity measurements

The porosity of neat CA is lower than 1% (see Table 2), indicating the formation of a tight and compact polymer matrix. The rise of porosity in the composite samples is a clear indication that materials synthesis resulted in the creation of nanoparticles. The transparency (at ∼600 nm) of the examined composite materials clearly drops with the addition of Au NPs, with sample S3 having high opacity (0.292%) and extremely low transparency (0.6%) in comparison with the pristine CA sample (transparency of 81.1% and opacity of 0.005%). Here, due to the sufficiently high nanoparticle load (but still very low Au content, as evidenced by EDX), localized plasmon resonance caused almost complete UV-light blocking. Interestingly, the preparation process yielded samples of almost uniform thickness, of around 130 μm.

Table 2 Thickness, transparency, opacity and porosity of neat CA and composite samples

Sample	Thickness/μm	Transparency/%	Opacity[a]/%	Porosity/%
CA	133	81.1	0.005	0.82
S1	129	49.9	0.039	9.79
S2	133	53.4	0.036	8.32
S3	129	0.6	0.292	8.25

[a] Materials with an opacity of 0.0 are considered to be fully transparent.

As illustrated in Fig. 7a, the neat CA exhibited a transmittance exceeding 80% across nearly the entire visible light spectrum, particularly within the red region (600 to 800 nm). On the other hand, the composite samples were significantly less transparent in the whole studied wavelength range. Specifically, samples S1 and S2 exhibited similar transmittance behaviour, both exceeding 50% in the range of 600 to 800 nm, while in the violet part of the spectra their transmittance is below 40%.

The trend of the observed transmittance and its correlation with the content of Au NPs highlight the importance of careful sample preparation when designing materials for specific optical applications. Accordingly, the absorbance spectra (Fig. 7b) revealed a broad peak within the 480–600 nm range, accompanied by a marked increase in absorbance around 400 nm, most notably in sample S3. Samples S1 and S2 follow a similar spectral trend, albeit with reduced intensity.

In addition, the UV region (340 nm to 450 nm) was studied more in detail using a dedicated UV lamp (see Fig. 8). Here, an almost complete transmittance (>95%) was observed in the case of the neat CA sample, whereas samples S1 and S2 showed a noticeable decrease in transmittance. Furthermore, sample S3 displayed almost no transmittance, indicating nearly complete absorption within the measured spectral range. These results emphasize the drastic change in optical behaviour of composites when a very small amount of Au NPs is present in the material, indicating their suitability for applications in wavelength-selective optical filtering. These results demonstrate that it is possible to achieve precise control over the optical properties by systematically adjusting the content of Au NPs within the CA polymer matrix, offering an adaptable platform for the development of advanced optoelectronic materials.

In the FTIR spectra (Fig. 9) several characteristic peaks are clearly noticeable. The most prominent are those around 1750 cm^{-1} corresponding to symmetric stretching of the
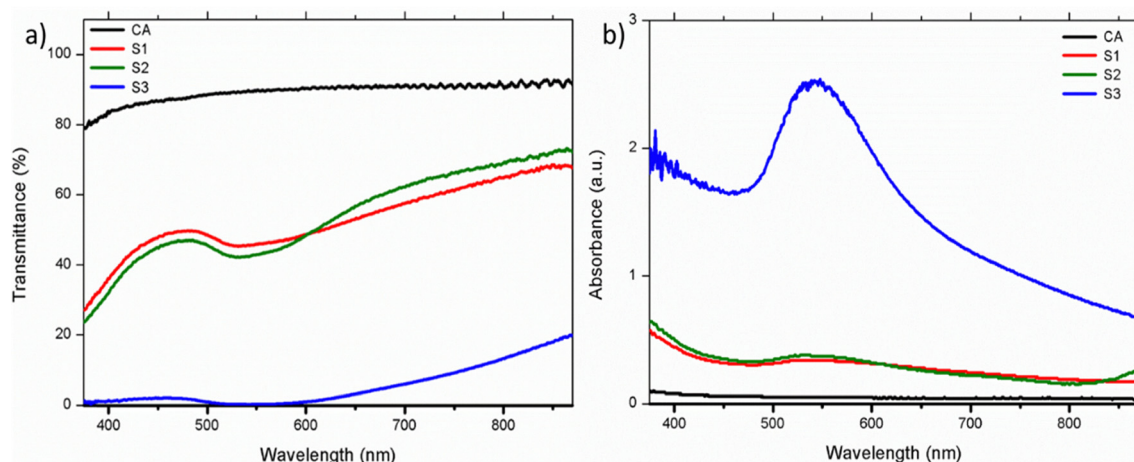
Fig. 7 UV-Vis spectra: (a) transmittance and (b) absorbance of neat CA and composite samples S1, S2, and S3.
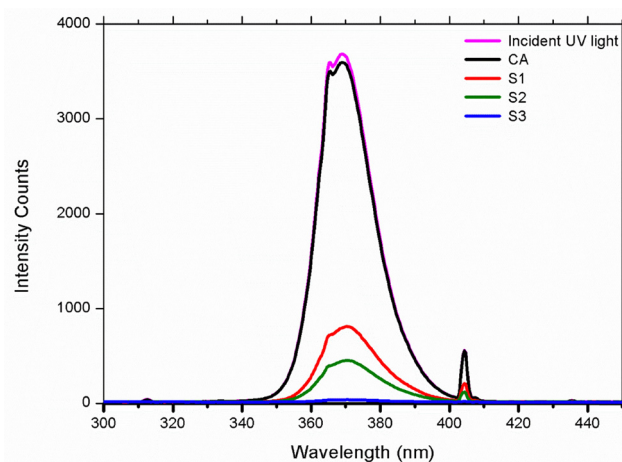

Fig. 8 UV spectra (transmittance) of neat CA and composite samples S1, S2 and S3. For comparison, the incident UV light intensity is also presented.
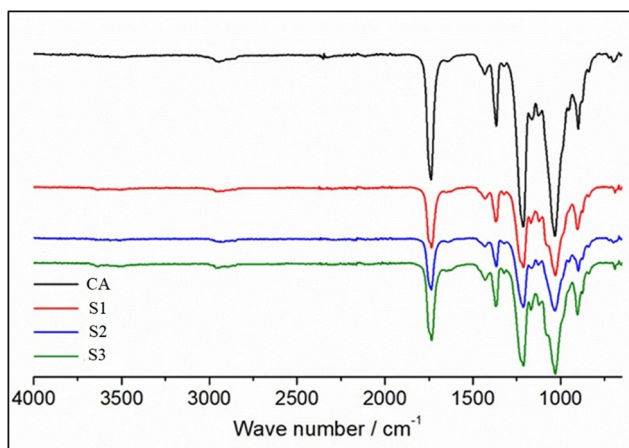

Fig. 9 FTIR analysis for the neat CA and composite samples S1, S2, and S3.

vibrations of the C–O bonds in acetyl groups (of CA). Small shifts and changes in intensities before the mentioned peaks in composite samples suggested interactions between the surface of the Au NPs and CA matrix.

The occurrence of Au–CA complexities is additionally confirmed by the broadening of peaks in the wavenumber range from 1052 to 1100 cm^{-1} as a result of the peaks overlapping and by intensity drop of peaks at 1430 cm^{-1} (–CH$_2$– deformation vibration), and 850 cm^{-1} (–C–O– stretching and –CH$_2$– rocking) in the composite samples. Outside the "fingerprint" region, characteristic bands around 3200–3500 cm^{-1} and those at around 2945 cm^{-1} were present, corresponding to the O–H stretching (absorbed water) and –CH$_2$– stretching in methylene groups, respectively.

Mechanical properties

The produced composites visibly demonstrate pronounced flexibility and mechanical robustness (as illustrated in Fig. 10), which is also supported by direct measurements of the Young's modulus.

The stress–strain curves of the axial tensile tests are shown in Fig. 11, while the Young's moduli are listed in Table 3. Axial tests have shown that the addition of Au NPs into the CA matrix
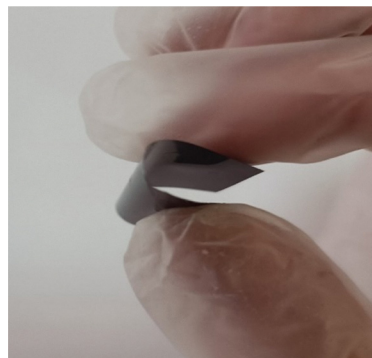

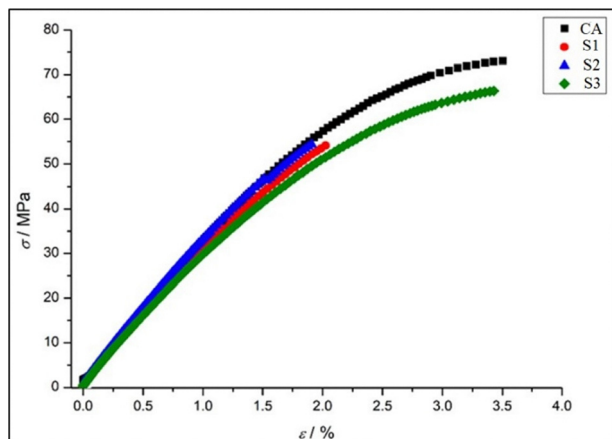**Fig. 10** Digital photograph of the bent composite sample S3.

carbonyl (C=O) of the acetyl group (CH$_3$C(O)O–) in CA, and those at around 1240 cm^{-1} and 1052 cm^{-1} representing

Fig. 11 Stress–strain diagram of the axial tensile tests for the neat CA and composite samples S1, S2, and S3.

Table 3 Results from the axial tensile tests

Sample	Young's modulus (E)/MPa
CA	31.71
S1	30.77
S2	31.86
S3	29.33

has a minimal impact on the Young's moduli of the materials for samples S1 and S2; only sample S3 showed a slightly lower value ($\sim 8\%$) compared to the neat CA.

Dynamic mechanical analyses of the materials showed that the addition of Au NPs to the CA matrix increased the storage and loss moduli in all cases (see Fig. 12a). Both the highest storage and loss moduli were achieved for sample S1, increasing the storage modulus by 49% and increasing the loss modulus by 62%.

The tan δ values are primarily of interest for obtaining the T_g (glass transition) of the materials: the T_g increases around 2 °C for all samples in our study (see Fig. 12b and Table 4). Based on the obtained tan δ values one can conclude that the addition of Au NPs into the CA matrix has a marginal impact on T_g.

Table 4 Glass transition temperatures of the tested materials

Sample	Glass transition temperature (T_g)/°C
CA	204.1
S1	206.7
S2	206.6
S3	206.6

Thermal behaviour

TGA was performed to evaluate the influence of Au NPs on the thermal stability of the samples and to assess the amount of the residue (Fig. 13). Both CA and all composites exhibit two degradation steps: one corresponded to the degradation of CA, and the other one to the degradation of the carbon residue. The addition of Au NPs had a minor effect on the thermal stability of the CA matrix, reducing the temperature of maximum degradation rate by up to 6 °C. However, the addition of Au NPs had a significant impact on reducing the stability of the carbon residue, lowering the temperature of the maximum degradation rate by up to 150 °C.

The residues at 700 °C after total degradation of the carbon residue are presented in Table 5. As expected, the neat CA has no residue while in the composite samples the residue ranges from 0.25% to 1.00% of starting mass. This can be attributed to Au NPs and other by-products of our modified Turkevich synthesis.

Next, a thorough DSC analysis was performed on all the samples (Table 6). The results indicated that the melting temperature (T_m) slightly decreased in the composite samples, in comparison with the neat CA. This was in contrast with the usual behaviour where T_m values rise as a more crystalline material is produced (see Fig. 1). Therefore, this could be due to the fact that the surface-to-volume ratio increased in the composites samples (as evidenced by SEM and AFM; see Fig. 2 and Fig. 4), leading to a drop of T_m values as a consequence of the improved free energy at the particle's surface.[59]

The cold crystallization (T_c) values rose as the Au NP content rose, indicating that the Au NPs acted positively as a surface
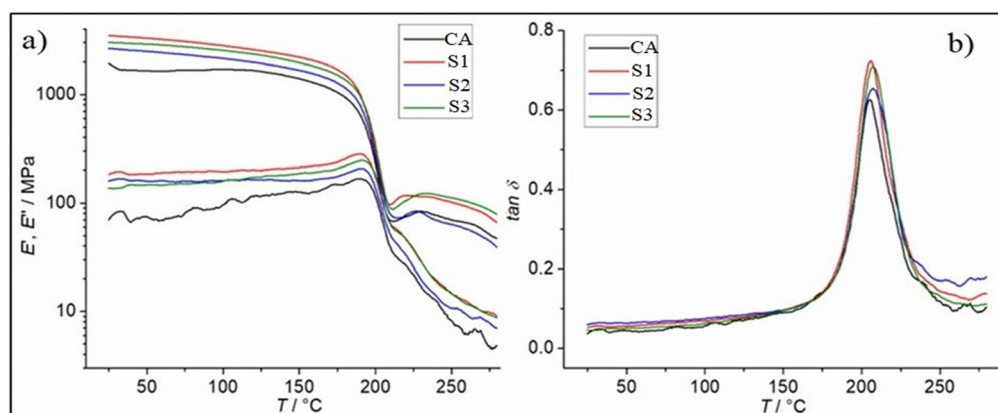

Fig. 12 DMA test results: (a) Set of lines representing the values of loss modulus E'', the upper being of storage modulus E'; (b) tan δ values of the DMA measurements.
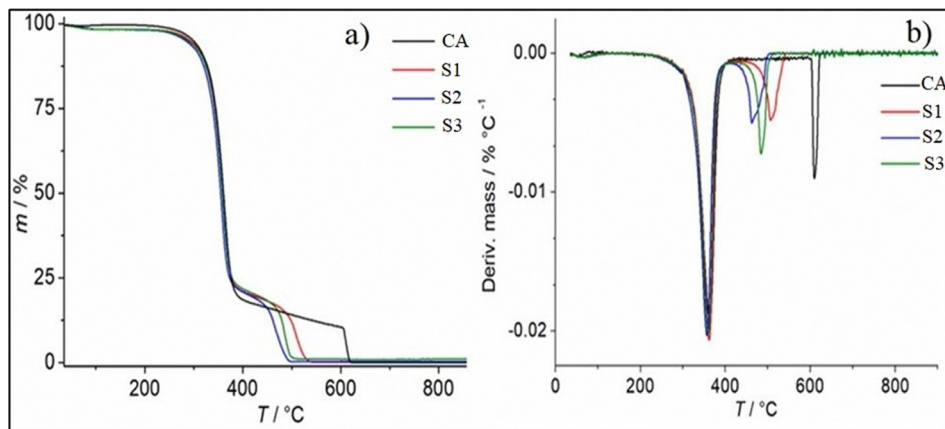
Fig. 13 Thermogravimetric (a) and differential thermogravimetric (b) curves for the neat CA and composite samples S1, S2, and S3.

Table 5 Mass% residues at 700 °C

Sample	1st measurement residue/%
CA	0.01
S1	0.25
S2	0.33
S3	1.00

Table 6 DSC results of neat CA and composite materials

Sample	T_m/°C	T_c/°C	ΔH_m/J g^{-1}	ΔH_c/J g^{-1}	X_c/%
CA	302.5	227.8	24.5	11.5	22.1
S1	301.4	227.5	23.8	9.9	23.7
S2	301.1	229.5	27.9	12.3	26.4
S3	301.4	228.8	22.7	8.9	23.4

nucleation agent.[60] However, these changes were minimal and non-linear, as were the changes of peak values of the crystallisation endotherms (ΔH_c). This, alongside the fact that the T_c and ΔH_c values showed an opposite trend in the case of sample S3, were indications that some local aggregation might still have occurred (individual structural characteristics of the tested samples). The calculated percent crystallinity (X_c) values correlate with the aforementioned tendencies. What is more, these results are in good agreement with the XRD measurements (Fig. 1) which also identified sample S2 having the highest crystallinity and the CA sample showing the lowest crystallinity.

Toxicity test: MTT assay

Considering the biomedical applications of the developed composites, evaluating its biocompatibility is essential. The cytotoxicity of composite samples was therefore assessed using the human fetal lung fibroblast cell line (MRC-5) and the MTT viability assay. Samples S1, S2 and S3 were tested and compared to neat CA as a control sample (Fig. 14). After a 48-hour incubation period, results showed a high cell viability rate, exceeding 80% at all tested samples (Fig. 15), including the sample S3 having the highest content of Au NPs (and other
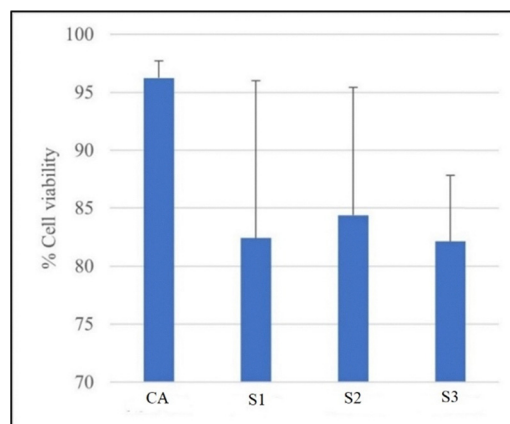

Fig. 14 Viability of MRC-5 cells following 48-hour incubation with composite samples S1, S2, and S3 analysed using an MTT survival assay. Data represent means ± standard deviation (SD) of three independent experiments. Control cells were incubated with neat CA.

by-products of the modified Turkevich method). These findings indicated that the synthesized composites did not exhibit significant cytotoxicity towards human fibroblast cells (MRC-5) under the tested conditions, supporting its potential for safe biomedical use, particularly in applications involving prolonged contact with human tissue, such as transdermal patches and wound dressings.

Conclusions

In this study, novel nanocomposites comprising Au NPs and CA were successfully synthesized using a modified Turkevich method and thoroughly characterized. These nanocomposites demonstrated favourable structural, mechanical, thermal, and optical properties, which, in combination with good biocompatibility, position them as promising candidates for advanced applications in transdermal drug delivery systems. Analysis of the composites indicated that Au NPs, even at very low concentrations, are homogeneously distributed throughout the CA
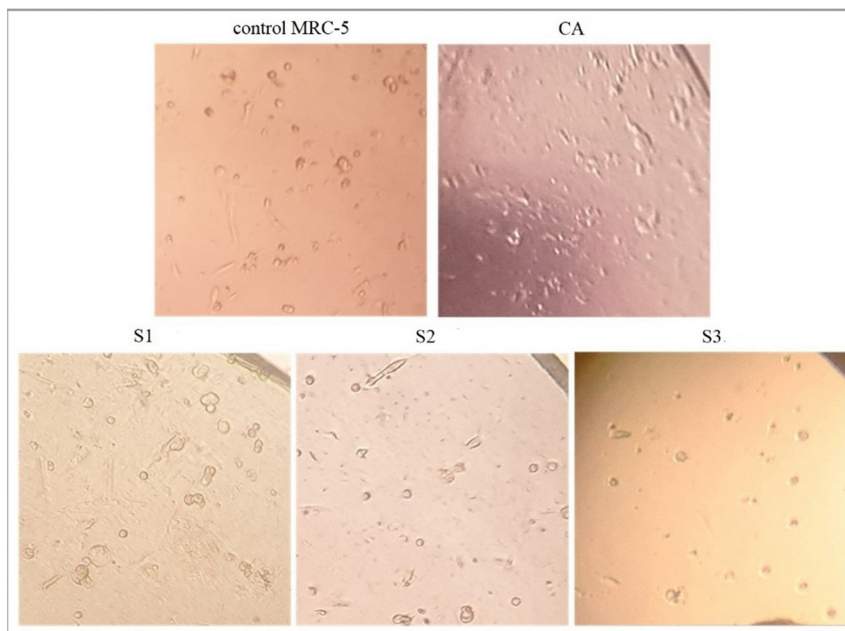
Fig. 15 Representative microscopy images of MRC-5 cells after a 48-hour incubation. Top row: untreated control cells (left) and cells incubated with neat CA discs (right). Bottom row: cells incubated with composites samples S1, S2, and S3.

matrix. This uniform dispersion exerts a pronounced influence on the functional properties of the material, most notably on its optical behaviour. The presence of dispersed Au NPs within the polymer CA matrix provides a versatile platform for the tailored fabrication of advanced optical filters. The mechanical and thermal characteristics of the composite remain closely aligned with those of the native CA matrix, which is consistent with the low doping levels of Au NPs. Importantly, the results of the MTT assay confirmed the low cytotoxicity and good biocompatibility of the nanocomposites towards human fibroblast cells (MRC-5), which experimentally underpins their suitability and safety for biomedical applications involving direct and prolonged tissue contact.

The promising results presented in this research underline the significant potential of the CA-Au NP composites in both nanotechnology and medicine. However, further research is essential to fully explore the optimization of production processes, scale-up techniques, and the long-term stability and safety of these nanocomposites. Future studies should focus on assessing biological interactions, pharmacokinetics, which are critical factors for their successful translation into clinical applications. With continued advancements in nanocomposite design and manufacturing, these materials could offer innovative solutions to some of the most pressing challenges in drug delivery, biosensing, and therapeutic treatments.

Author contributions

Mislav Mustapić: conceptualization, funding acquisition, supervision, investigation, formal analysis, writing – original draft, project administration. Maja Molnar: investigation, resources, writing – original draft. Nikola Španić: investigation, resources, writing – original draft. Mario Komar: investigation. Barbara Viljetić: investigation, resources, writing – original draft. Ljubica Glavaš-Obrovac: supervision, funding acquisition. Marija Heffer: supervision, funding acquisition. Boštjan Genorio: investigation, resources, writing – original draft. Ana Ivković: investigation. Rafael Anelić: investigation. Fabio Faraguna: investigation, resources, writing – original draft. Lázár Tóth: investigation. Judit Budai: investigation. Zsuzsanna Márton: investigation, supervision. Domagoj Belić: funding acquisition, writing – review & editing, visualization, formal analysis, investigation.

Conflicts of interest

The authors declare that they have no competing interests relevant to the content of this article.

Data availability

The data supporting the findings of this study are available from the corresponding authors upon reasonable request.

Acknowledgements

References

1 A. Adhikari, S. Mondal, S. Darbar and S. Kumar Pal, Role of nanomedicine in redox mediated healing at molecular level, *Biomol. Concepts*, 2019, **10**, 160–174, DOI: **10.1515/bmc-2019-0019**.

2 F. Din, W. Aman, I. Ullah, O. S. Qureshi, O. Mustapha, S. Shafique and A. Zeb, Effective use of nanocarriers as drug delivery systems for the treatment of selected tumors, *Int. J. Nanomed.*, 2017, **12**, 7291–7309, DOI: **10.2147/ijn.s146315**.

3 S. Roig-Sanchez, E. Jungstedt, I. Anton-Sales, D. C. Malaspina, J. Faraudo, L. A. Berglund, A. Anna Laromaine and A. Roig, Nanocellulose films with multiple functional nanoparticles in confined spatial distribution, *Nanoscale Horiz*, 2019, **4**, 634, DOI: **10.1039/c8nh00310f**.

4 M. Mustapić, Z. Glumac, M. Heffer, M. Zjalić, I. Prološćić, M. Masud, S. Blažetić, A. Vuković, M. Billah, A. Khan and S. Šegota, Al Hossain Md Sh; AC/DC magnetic device for safe medical use of potentially harmful magnetic nanocarriers, *J. Hazard Mater.*, 2021, **409**, 124918, DOI: **10.1016/j.jhazmat.2020.124918**.

5 M. D'Acunto, P. Cioni, E. Gabellieri and G. Presciuttini, Exploiting gold nanoparticles for diagnosis and cancer treatments, *Nanotechnology*, 2021, **32**(19), 192001, DOI: **10.1088/1361-6528/abe1ed**.

6 E. Boisselier and D. Astruc, Gold Nanoparticles in Nanomedicine: Preparations, Imaging, Diagnostics, Therapies and Toxicity, *Chem. Soc. Rev.*, 2009, **38**(6), 1759–1782, DOI: **10.1039/B806051G**.

7 A. Munire, Z. Kebing, Z. Jun, Z. Huaping and L. Feng, Anti-inflammatory role of gold nanoparticles in the prevention and treatment of Alzheimer's disease, *J. Mater. Chem. B*, 2023, **11**, 8605–8621, DOI: **10.1039/D3TB01023F**.

8 E. C. Dreaden, A. M. Alkilany, X. Huang, C. J. Murphy and M. A. El-Sayed, The Golden Age: Gold Nanoparticles for Biomedicine, *Chem. Soc. Rev.*, 2012, **41**(7), 2740–2779, DOI: **10.1039/C1CS15237H**.

9 M. Razzaghi, A. Homaei, R. Hemmati, D. Saberi and S. Kavousipour, Cellulose-gold nanohybrid as an effective support to enhance the catalytic efficiency and stability of α-amylase from Bacillus aquimaris, *J. Mol. Liq.*, 2023, **391**, 123399, DOI: **10.1016/j.molliq.2023.123399**.

10 X. Wu, C. Lu, Z. Zhou, G. Yuan, R. Xiong and X. Zhang, Green synthesis and formation mechanism of cellulose nanocrystal-supported gold nanoparticles with enhanced catalytic performance, *Environ. Sci.:Nano*, 2014, **1**(1), 71–79, DOI: **10.1039/C3EN00066D**.

11 B. D. Chithrani, A. A. Ghazani and W. C. W. Chan, Determining the Size and Shape Dependence of Gold Nanoparticle Uptake into Mammalian Cells, *Nano Lett.*, 2006, **6**(4), 662–668, DOI: **10.1021/nl052396o**.

12 L. Dykman and N. Khlebtsov, Gold Nanoparticles in Biomedical Applications: Recent Advances and Perspectives, *Chem. Soc. Rev.*, 2012, **41**(6), 2256–2282, DOI: **10.1039/C1CS15166E**.

13 C. R. Cabreira, F. T. da Silva and F. F. Camilo, Cellulose Film-Integrated Gold Nanoparticles Synthesized in Ionic Liquids for Heterogeneous Catalysis, *ACS Appl. Nano Mater.*, 2024, **7**(12), 14796–14804, DOI: **10.1021/acsanm.4c02647**.

14 J. Yu, W. Li, Q. Li, P. Li, A. V. Rogachev, X. Jiang and J. Yang, Highly Efficient Continuous Flow Nanocatalyst Platform Constructed with Regenerable Bacterial Cellulose Loaded with Gold Nanoparticles and a Nanoporous Membrane, *Langmuir*, 2024, **40**(37), 19548–19559, DOI: **10.1021/acs.langmuir.4c02045**.

15 N. Pazos-Perez, L. Guerrini and R. A. Alvarez-Puebla, Plasmon Tunability of Gold Nanostars at the Tip Apexes, *ACS Omega*, 2018, **3**(12), 17173–17179, DOI: **10.1021/acsomega.8b02686**.

16 C. Wang, X.-G. Nie, Y. Shi, Y. Zhou, J.-J. Xu, X.-H. Xia and H.-Y. Chen, Direct Plasmon-Accelerated Electrochemical Reaction on Gold Nanoparticles, *ACS Nano*, 2017, **11**(6), 5897–5905, DOI: **10.1021/acsnano.7b01637**.

17 J. Guo, I. Filpponen, P. Su, J. Laine and O. J. Rojas, Attachment of gold nanoparticles on cellulose nanofibrils via click reactions and electrostatic interactions, *Cellulose*, 2016, **23**(5), 3065–3075, DOI: **10.1007/s10570-016-1042-7**.

18 M. R. K. Ali, Y. Wu and M. A. El-Sayed, Gold-Nanoparticle-Assisted Plasmonic Photothermal Therapy Advances Toward Clinical Application, *J. Phys. Chem. C*, 2019, **123**(25), 15375–15393, DOI: **10.1021/acs.jpcc.9b01961**.

19 C. Kunstmann-Olsen, D. Belic, D. F. Bradley, M. P. Grzelczak and M. Brust, Humidity-Dependent Reversible Transitions in Gold Nanoparticle Superlattices, *Chem. Mater.*, 2016, **28**(9), 2970–2980, DOI: **10.1021/acs.chemmater.6b00070**.

20 J. Van Rie and W. Thielemans, Cellulose–gold nanoparticle hybrid materials, *Nanoscale*, 2017, **9**(25), 8525–8554, DOI: **10.1039/C7NR00400A**.

21 J. Zhao, Z. Lu, M. Shao, D. Yan, M. Wei, D. G. Evans and X. Duan, Flexible hierarchical nanocomposites based on MnO$_2$ nanowires/CoAl hydrotalcite/carbon fibers for high-performance supercapacitors, *RSC Adv.*, 2013, **3**, 1045, DOI: **10.1039/C2RA22566B**.

22 J. Xu, H. Yang, Z. Luo, D. Wu and C. Gengyu, Synergistic effects of core@double-shell structured magnesium hydroxide microcapsules on flame retardancy and smoke suppression in flexible poly(vinyl chloride), *RSC Adv.*, 2022, **12**, 2914, DOI: **10.1039/D1RA09030E**.

23 G. Biagiotti, R. Cazzoli, P. Andreozzi, G. Aresta, M. Francesco, C. Mangini, P. di Gianvincenzo, C. Tobia, S. Recchia, L. Polito, M. Severi, O. Vittorio, S. Cicchi,

S. E. Moya, R. Ronca, A. Albini, D. Berti, R. Orecchia, C. Garibaldi, S. Minucci and B. Richichi, Biocompatible cellulose nanocrystal-based Trojan horse enables targeted delivery of nano-Au radiosensitizers to triple negative breast cancer cells, *Nanoscale Horiz.*, 2024, **9**, 1211–1218, DOI: **10.1039/d4nh00042k**.

24 M. N. Norizan, S. S. Shazleen, A. H. Alias, F. A. Sabaruddin, M. R. M. Asyraf, E. S. Zainudin, N. Abdullah, M. S. Samsudin, S. H. Kamarudin and M. N. F. Norrrahim, Nanocellulose-Based Nanocomposites for Sustainable Applications: A Review, *Nanomaterials*, 2022, **12**(19), 3483, DOI: **10.3390/nano12193483**.

25 K. Dhali, M. Ghasemlou, F. Daver, P. Cass and B. Adhikari, A Review of Nanocellulose as a New Material towards Environmental Sustainability, *Sci. Total Environ.*, 2021, **775**, 145871, DOI: **10.1016/j.scitotenv.2021.145871**.

26 C. M. Kinoan and H. Katas, Sustainable production and antibacterial efficacy of silver nanoparticles on cellulose nanofibers from mushroom waste, *RSC Adv.*, 2025, **15**, 19726–19740, DOI: **10.1039/d5ra02087e**.

27 N. Španić, V. Jambreković, M. Šernek and S. Medved, Influence of natural fillers on thermal and mechanical properties and surface morphology of cellulose acetate-based biocomposites, *Int. J. Polym. Sci.*, 2019, **1065024**, 17, DOI: **10.1155/2019/1065024**.

28 A. Ach, Biodegradable plastic based on cellulose acetate, *J. Macromol. Sci., Part A: Pure Appl. Chem.*, 1993, **30**(9–10), 733–740, DOI: **10.1080/10601329308021259**.

29 A. Rezaei, A. Nasirpour and M. Fathi, Application of cellulosic nanofibers in food science using electrospinning and its potential risk, *Compr. Rev. Food Sci. Food Saf.*, 2015, **14**(3), 269–284, DOI: **10.1111/1541-4337.12128**.

30 O. Eskilson, S. B. Lindström, B. Sepulveda, M. M. Shahjamali, P. Güell-Grau, P. Sivlér, M. Skog, C. Aronsson, E. M. Björk, N. Nyberg, H. Khalaf, T. Bengtsson, J. James, M. B. Ericson, E. Martinsson, R. Selegård and D. Aili, Self-Assembly of Mechanoplasmonic Bacterial Cellulose–Metal Nanoparticle Composites, *Adv. Funct. Mater.*, 2020, **30**(40), 2004766, DOI: **10.1002/adfm.202004766**.

31 A. H. Tayeb, E. Amini, S. Ghasemi and M. Tajvidi, Cellulose Nanomaterials—Binding Properties and Applications: A Review, *Molecules*, 2018, **23**(10), 2684, DOI: **10.3390/molecules23102684**.

32 C. Salas, T. Nypelö, C. Rodriguez-Abreu, C. Carrillo and O. J. Rojas, Nanocellulose properties and applications in colloids and interfaces, *Curr. Opin. Colloid Interface Sci.*, 2014, **19**(5), 383–396, DOI: **10.1016/j.cocis.2014.10.003**.

33 Z. Wei, Y. Huang, D. Zhao, Z. Hu, Z. Li and Z. Liang, A Pliable Electroporation Patch (ep-Patch) for Efficient Delivery of Nucleic Acid Molecules into Animal Tissues with Irregular Surface Shapes, *Sci. Rep.*, 2015, **5**, 7618, DOI: **10.1038/srep07618**.

34 R. Ajdary, S. Huan, N. Zanjanizadeh-Ezazi, W. Xiang, R. Grande, H. A. Santos and O. J. Rojas, Acetylated Nanocellulose for Single-Component Bioinks and Cell Proliferation on 3D-Printed Scaffolds, *Biomacromolecules*, 2019, **20**, 2770–2778, DOI: **10.1021/acs.biomac.9b00527**.

35 D. Zhao, Y. Zhu, W. Cheng, W. Chen, Y. Wu and H. Yu, Cellulose-Based Flexible Functional Materials for Emerging Intelligent Electronics, *Adv. Mater.*, 2021, **33**(28), 2000619, DOI: **10.1002/adma.202000619**.

36 W. Chen, H. Yu, S.-Y. Lee, T. Wei, J. Li and Z. Fan, Nanocellulose: A Promising Nanomaterial for Advanced Electrochemical Energy Storage, *Chem. Soc. Rev.*, 2018, **47**(8), 2837–2872, DOI: **10.1039/C7CS00790F**.

37 H. Seddiqi, E. Oliaei, H. Honarkar, J. Jin, L. C. Geonzon, R. G. Bacabac and J. Klein-Nulend, Cellulose and its Derivatives: towards Biomedical Applications, *Cellulose*, 2021, **28**(4), 1893–1931, DOI: **10.1007/s10570-020-03674-w**.

38 Y. Huo, Y. Liu, M. Xia, H. Du, Z. Lin, B. Li and H. Liu, Nanocellulose-Based Composite Materials Used in Drug Delivery Systems, *Polymers*, 2022, **14**(13), 2648, DOI: **10.3390/polym14132648**.

39 S. W. A. Shah, L. Xingxing, H. Yuan, H. Shen, S. Quan, G. Pan, M. Ishfaq, A. U. Shah, H. Xie and J. Shaoc, Innovative transdermal drug delivery systems: Benefits, challenges, and emerging application, *BMEMat*, 2025, DOI: **10.1002/bmm2.70001**.

40 X. Xie, C. Pascual, C. Lieu, S. Oh, J. Wang, B. Zou, J. Xie and Z. Li, Analgesic Microneedle Patch for Neuropathic Pain Therapy, *ACS Nano*, 2017, **11**, 395, DOI: **10.1021/acsnano.6b06104**.

41 H. Wei, K. Rodriguez, S. Renneckar, W. Leng and P. J. Vikesland, Preparation and evaluation of nanocellulose–gold nanoparticle nanocomposites for SERS applications, *Analyst*, 2015, **140**(16), 5640–5649, DOI: **10.1039/C5AN00606F**.

42 B. Demir, K.-Y. Chan, D. Yang, A. Mouritz, H. Lin, B. Jia, K.-T. Lau and T. R. Walsh, Epoxy-gold nanoparticle nanocomposites with enhanced thermo-mechanical properties: An integrated modelling and experimental study, *Compos. Sci. Technol.*, 2019, **174**, 106–116, DOI: **10.1016/j.compscitech.2019.02.020**.

43 L. D. Villa-García, R. Márquez-Preciado, M. Ortiz-Magdaleno, O. A. Patrón-Soberano, M. A. Álvarez-Pérez, A. Pozos-Guillén and L. O. Sánchez-Vargas, Antimicrobial effect of gold nanoparticles in the formation of the Staphylococcus aureus biofilm on a polyethylene surface, *Braz. J. Microbiol.*, 2021, **52**(2), 619–625, DOI: **10.1007/s42770-021-00455-w**.

44 N. Španić, V. Jambreković and M. Klarić, Basic chemical composition of wood as a parameter in raw material selection for biocomposite production, *Cellul. Chem. Technol.*, 2018, **52**(3–4), 163–169.

45 Technical Association of the Pulp and Paper Industry, Sampling and preparation of wood for analysis, TAPPI Method T 257 cm-12, TAPPI Press, Atlanta, 2012.

46 Technical Association of the Pulp and Paper Industry, Solvent extractives of wood and pulp, TAPPI Method T 204 cm-97, TAPPI Press, Atlanta, 1997.

47 M. Mustapić, I. Vrdoljak, I. Miličević, M. Molnar, S. Rupčić, N. Španić, B. Genorio, M. Komar, Ž. Skoko and F. Faraguna, Synthesis of silver cellulose-acetate composite for EMI shielding applications, *J. Mater. Sci.: Mater. Electron.*, 2025, **36**(142), DOI: **10.1007/s10854-024-14171-2**.

48 ASTM, *Annual Book of ASTM Standards - ASTM D 817–96– Standard test methods of testing cellulose acetate propionate and cellulose acetate butyrate*, ASTM International, West Conshohocken, PA, USA, 2010.

49 J. Turkevich, P. C. Stevenson and J. Hillier, A study of the nucleation and growth processes in the synthesis of colloidal gold, *Discuss. Faraday Soc.*, 1951, **11**, 55–75, DOI: **10.1039/DF9511100055**.

50 D. A. Cerqueira, G. R. Filho and R. M. N. Assunção, A new value for the heat of fusion of a perfect crystal of cellulose acetate, *Polym. Bull.*, 2006, **56**, 475–484, DOI: **10.1007/s00289-006-0511-947**.

51 C. F. Wang, Y. An, Q. H. Li, S. J. Wan, W. X. Chen and X. D. Liu, Nonsolvent effects on morphology of cellulose acetate films prepared by dry-cast process, *J. Macromol. Sci. B*, 2012, **51**(11), 2266–2275, DOI: **10.1080/00222348.2012.67230**.

52 T. Mosmann, Rapid colorimetric assay for cellular growth and survival: Application to proliferation and cytotoxicity assays, *J. Immunol. Methods*, 1983, **65**(1–2), 55–63, DOI: **10.1016/0022-1759(83)90303-4**.

53 V. Žepič, I. Poljanšek, P. Oven, A. Sever Škapin and A. Hančič, Effect of Drying Pretreatment on the Acetylation of Nanofibrillated Cellulose, *BioResources*, 2015, **10**(4), 8148–8167, DOI: **10.15376/biores.10.4.8148-8167**.

54 J. Drożdżek, J. Zawadzki, T. Zielekiewicz, T. Kłosińska, J. Gawron, T. Gołofit and S. Borysiak, The Influence of Method of Cellulose Isolation from Wood on the Degree and Index of Crystallinity, *Wood Res.*, 2015, **60**(2), 255–262.

55 B. Mohebby, Application of ATR Infrared Spectroscopy in Wood Acetylation, *J. Agric. Sci. Technol.*, 2008, **10**, 253–259.

56 N. Španić, V. Jambreković, S. Medved and A. Antonović, Chemical and Thermal Properties of Cellulose Acetate Prepared from White Willow (Salix alba) and Black Alder (Alnus Glutinosa) as a Potential Polymeric Base of Biocomposite Materials, *Chem. Biochem. Eng. Q.*, 2015, **29**(3), 357–365, DOI: **10.15255/CABEQ.2015.2176**.

57 M. Wuithschick, A. Birnbaum, S. Witte, M. Sztucki, U. Vainio, N. Pinna, K. Rademann, F. Emmerling, R. Kraehnert and J. Polte, Turkevich in New Robes: Key Questions Answered for the Most Common Gold Nanoparticle Synthesis, *ACS Nano*, 2015, **9**(7), 7052–7071, DOI: **10.1021/acsnano.5b01579**.

58 J. Dong, P. L. Carpinone, G. Pyrgiotakis, P. Demokritou and B. M. Moudgi, Synthesis of Precision Gold Nanoparticles Using Turkevich Method, *KONA*, 2020, **37**, 224–232, DOI: **10.14356/kona.2020011**.

59 J.-H. Shim, B.-J. Lee and Y. W. Cho, Thermal stability of unsupported gold nanoparticle: a molecular dynamics study, *Surf. Sci.*, 2002, **512**, 262–268, DOI: **10.1016/S0039-6028(02)01692-8**.

60 C. deArmitt and M. Hancock, In Filled Thermoplastics, *Particulate-Filled Polymer Composites*, 2nd edn, ed R. N. Rothon, Rapra Technology Limited, UK, pp. 357–424, 2003.